Journal of Nanoparticle Research (2022) 24:248
https://doi.org/10.1007/s11051-022-05611-3

RESEARCH PAPER

Flash evaporation of low volatility solid precursors by a scanning infrared laser

Jeremias Geiss · Jeldrik Schulte · Markus Winterer

Received: 23 June 2022 / Accepted: 28 October 2022 / Published online: 25 November 2022

Abstract The steady and stoichiometric delivery of metal-organic precursor mixtures is essential for the production of complex, functional nanomaterials in the gas phase. Chemical vapor synthesis (CVS) is a corresponding process which enables the production of complex oxide nanoparticles such as perovskites. While there exist a vast number of compositions that form perovskite structures, many technically relevant materials consist of transition metals and lanthanides. Their corresponding metal organic precursors often deviate significantly in their thermal behavior, resulting in a challenging delivery of precursors to the reactor. One suitable method for precursor delivery is flash evaporation by an infrared laser, where a mixture of solid precursors is instantly sublimed. Using flash evaporation, the stoichiometry of the generated vapor corresponds to the composition of precursors in the solid mixture. In this study, we present an alternative flash evaporation system based on a marking laser which rapidly scans a focused infrared beam across a precursor powder bed. By focusing the beam, higher energy densities are reached, compared to existing systems while a large area powder bed is repeatedly scanned and sublimed. Fourier-transform infrared spectroscopy (FTIR) measurements confirm the decomposition-free sublimation of precursor mixtures. Furthermore, we confirm the successful precursor delivery by the synthesis of $LaFeO_3$ nanoparticles with an average crystallite size of 5.3 nm. The structure of the ensemble of nanoparticles is examined using X-ray diffraction (XRD) and Rietveld refinement, transmission electron microscopy (TEM), selected area diffraction (SAED), and extended X-ray absorption fine structure (EXAFS) at the Fe-K edge analyzed by reverse Monte Carlo (RMC) analysis.

Keywords Synthesis · Nanoparticles · Gas phase · Perovskite · Aerosols

J. Geiss (✉) · J. Schulte · M. Winterer
Nanoparticle Process Technology (NPPT) and Center for Nanointegration Duisburg-Essen (CENIDE), University of Duisburg-Essen, Lotharstr. 1, Duisburg, 47057, NRW, Germany
e-mail: jeremias.geiss@uni-due.de

Introduction

Nanocrystalline oxides are applied for example as photocatalysts and gas sensors [1, 2]. While there exist several gas-phase processes for their syntheses, most setups consist of three stages which are a delivery of precursors and gases, a reaction zone where particles are formed and a system to collect the participles [3, 4]. Chemical vapor synthesis (CVS) is a gas-phase process that corresponds to this scheme [5]. In CVS, metal-organic precursors are provided as diluted vapors in a carrier gas and mixed with oxygen. In a sequential reactor, the precursor decomposes,

followed by nucleation and growth of nanoparticles. Short reaction times and hot reaction zones result in highly crystalline ensembles of nanoparticles. The composition of the precursor vapor corresponds to the stoichiometry of synthesized nanoparticles and allows the production of defined complex oxide phases.

Liquid precursors may be precisely dosed by temperature controlled bubbler systems [6]. However, liquid metal organic precursors are often toxic and flammable, e.g., iron pentacarbonyl. Furthermore, only few liquid rare-earth metal organic precursors are available. Solid metal organic precursors in powderous form, e.g., metal acetylacetonates are less volatile, but widely available and often safer to handle. One method to deliver precise doses of metal organic precursor vapors including mixtures from solid precursor powders is laser-flash-evaporation [7–10]. The precursor delivery is also used in the related chemical vapor deposition (CVD) to produce high-quality layers [11]. This delivery system consists of an expanded infrared laser beam which irradiates a powder mixture of solid precursors. The principle is based on non-equilibrium evaporation, where the precursors sublimes instantly upon irradiation. Consequentially, the molar composition of the generated vapor corresponds to the composition of the powder bed. Therefore, flash evaporation enables the stoichiometric delivery of precursor mixtures with significantly different evaporation or sublimation dynamics.

Current flash evaporation setups consist of infrared lasers combined with beam expanding optics where a powder bed of solid precursors is passed through the expanded beam. Furthermore, existing setups operate at high laser powers and narrow beam expansion ratios to provide a beam of high power density that leads to flash evaporation instead of heat dissipation.

In this study, we present a new flash evaporator that is based on a focused yet lower power, scanning IR laser that sublimes metal organic precursors of a large area powder bed. To verify the applicability of the focused laser beam for flash-evaporation, the irradiated precursor is examined for structural decomposition and the evaporation rates are determined. A CVS synthesis is conducted to benchmark the precursor delivery and to produce $LaFeO_3$ nanoparticles from 2,4-pentanedione iron(III) ($Fe(acac)_3$) and 2,2,6,6-tetramethyl-3,5-heptanedionate(III)lanthanum ($La(tmhd)_3$). Stoichiometric evaporation is challenging since $Fe(acac)_3$ is significantly more volatile which is indicated by its lower sublimation enthalpy of ΔH_{sub} = 112 kJmol^{-1} [12] compared to ΔH_{sub} = 155 kJmol^{-1} [13] of ($La(tmhd)_3$) and by differences in their thermal gravimetric analysis (TGA) profiles [14]. The synthesized particles are examined using X-ray diffraction (XRD) with Rietveld refinement, transmission electron microscopy (TEM) imagery, and diffraction. Finally, extended X-ray absorption fine structure (EXAFS) at the Fe-K edge measurements with reverse Monte Carlo (RMC) analysis is applied to examine the local structure for the nanoparticles.

Conceptual idea and technical realization

Existing versions of laser flash evaporator systems consist of an infrared laser with a lens system to expand the beam onto a powder bed of solid precursors as illustrated in Fig. 1a. The mixture of metal organic compounds in the powder bed is hit by intense IR laser irradiation and instantly sublimes. Then, a steady stream of carrier gas transports the vapor to a reactor. The flash evaporator presented in the current study is driven by a different working principle. It consists of a marking head which scans a focused laser beam across the powder bed (Fig. 1b). The laser beam is moved by galvanometers and a f-theta lens generates a flat focal plane. Therefore, a large area of the powder bed is covered by the laser while the focused beam leads to an increased power density. The flash evaporator setup consists of a commercial 48 W CO_2-laser (Firestar v40, Synrad) with a wavelength of 10.6 μm and a marking head (FH Flyer, Synrad) that is equipped with a f-theta focus lens with a focal length of 200 mm. The focused beam has a diameter of 300 µm, a maximum power density of 600 W/mm^2, and is scanned at a speed of up to 7620 mm/s across the focal plane. The laser beam enters the vacuum vessel through a ZnSe window that is flushed with a steady stream of helium to avoid deposition of precursors. The beam and flushing gas enter the main chamber through an oblong hole which acts as an orifice for the gas and as a feedthrough for the laser beam. A sequential, flat powder bed of precursor is aligned to the focal plane of the laser and mounted on a movable stage which is driven by a trapezoidal screw and a stepper motor. This drive moves the precursor powder along the axis of the trapezoidal screw as indicated

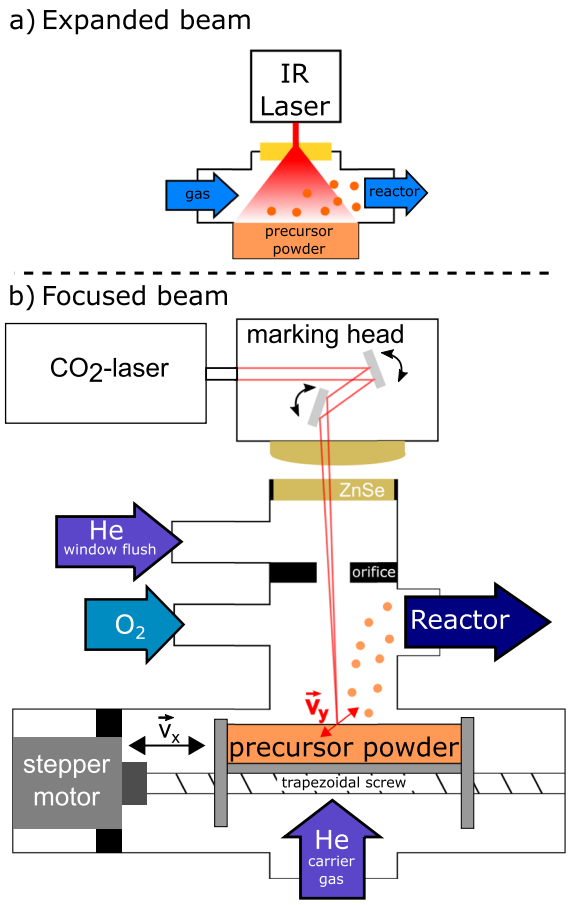

Fig. 1 (a) Working principles of existing flash-evaporators by a laser with beam expansion and (b) illustration of the novel flash-evaporator with a scanning head

by $\vec{v}_x$. Simultaneously, the beam is scanned in a perpendicular line as indicated by $\vec{v}_y$. Both movements result in a pattern of continuous lines that are written into the powder bed as shown by Fig. 2a. Helium is injected into evaporator from the bottom which carriers the generated vapors from the precursor boat to the outlet where the vapors are mixed with pre-heated oxygen before the mixture enters a subsequent reactor.

Experimental methods

A scheme for the CVS process with the newly developed flash evaporator for the synthesis of $LaFeO_3$ nanoparticles is provided in Fig. 7 in the Appendix.

The laser and marking head of the precursor delivery operates at a duty cycle of 25%, a frequency of 20 kHz and a scanning speed of $\vec{v}_y$ = 361 mm/s. The precursor boat moves continuously at a speed of $\vec{v}_x$ = 2.5 mm/s and is filled with a stoichiometric precursor mixture of $Fe(acac)_3$ and $La(tmhd)_3$. The incoming gas stream consist of 200 sccm of helium for the window flush, 800 sccm of helium as carrier gas, and 1000 sccm of oxygen which is heated to 523 K. The subsequent hot wall reactor consists of an alumina tube (1 m length, inner diameter 18 mm) inside a tube furnace that is heated to 1473 K. Downstream, a thermophoretic particle collector separates the nanoparticles from the remaining gas. The constant pressure of 20 mbar in the reactor is controlled by a butterfly valve connected to a screw pump.

Absorbance spectra of pristine and flash-evaporated precursors are recorded by a Vertex 80 FTIR spectrometer with Platinum ATR attachment from 4000 to 400 cm^{-1} with a resolution of 4 cm^{-1}. For the FTIR measurement, the flash-evaporated precursor vapors are deposited in a quartz-tube which is mounted sequentially to the flash-evaporator. Evaporation rates are determined gravimetrically from the residual precursor after the completion of an evaporation cycle.

X-ray diffraction measurements of the synthesized $LaFeO_3$ nanoparticles are performed at the P02.1 beamline [15] at the DESY synchrotron at room temperature and a wavelength of (λ = 0.2073 Å). The powder samples are enclosed inside a 0.5 mm special glass capillary tube and measured in transmission by a Varex XRD 4343CT detector. The sample to detector distance, detector tilt, and beam center are determined using a diffraction pattern of a LaB_6 660c NIST standard reference and the package DIOPTAS [16]. The instrumental function is determined and the integrated datasets (0.7 $Å^{-1} < Q < 8.5$ $Å^{-1}$) are analyzed by Rietveld refinement using the software package PROFEX [17] to refine crystal lattice parameters, crystallite size, and microstrain.

X-ray absorption spectra are measured in transmission at the Fe-K edge (7112 eV) at the 20 BM beamline [18] at the Advanced Photon Source of Argonne National Laboratory, USA. The nanoparticles are diluted in starch and pressed uniaxially into pellets. The absolute energy scale is calibrated by a simultaneous measurement of a standard Fe metal foil.

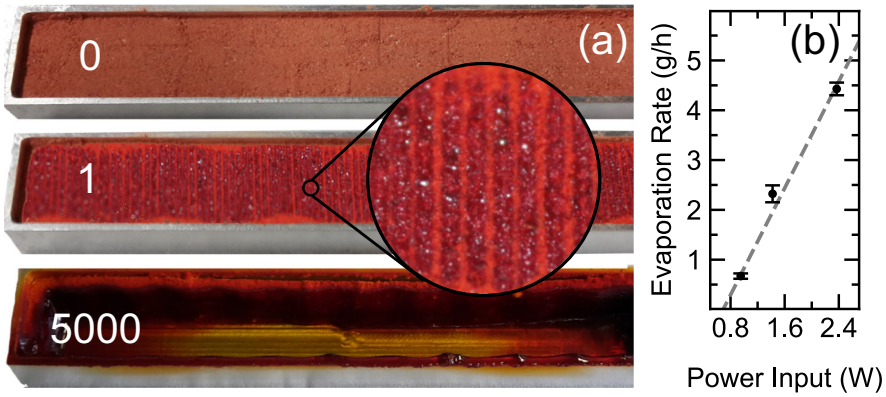

Fig. 2 (a) Comparison of the powder bed which contains a mixture of $Fe(acac)_3$ and $La(tmhd)_3$ after a defined number of laser cycles. Enlarged section shows molten material of laser irradiated area. (b) Evaporation rate as a function of the average power input

EXAFS is extracted using the xafsX [19] package. EXAFS datasets are processed by the reverse Monte Carlo (RMC) program rmcxas in k-space (0–14 $Å^{-1}$) [20]. Theoretical phase and amplitude functions are calculated by the FEFF 8 code [21]. The initial RMC model is based on the site symmetry and lattice parameters from the Rietveld refinement of the XRD data and consist of a $LaFeO_3$ sphere with a diameter of 5.2 nm inside a simulation box with an edge length of 10 nm. The coordination number N, radial distance R and the mean square displacement σ^2 are determined from a moment analysis of the partial pair distribution functions.

Results and discussion

Flash-evaporation of precursors

Figure 2 shows images of the precursor mixture inside the evaporation boat in the pristine state and after the laser has scanned the powder bed for one cycle and for 5000 cycles. A row of sequential lines are visible in the powder bed after the first cycle. The magnified view of the lines reveals that the laser beam leads to a densification of the precursor in the boat which results in a change of color, without indication for a decomposition. After 5000 cycles, the precursor mixture is completely sublimed and only a small residual film of precursor is left inside the aluminum evaporation boat. The focused laser of the scanning head creates power densities of 10^5 W/cm^2 on the precursor bed which is significantly higher than previously existing setups with 10^3 W/cm^2. For the CVS process, the precursor must be delivered to the reactor without decomposition. FTIR measurements are conducted to determine if the increased power density results in a decomposition of the precursor. Figure 3 shows the IR fingerprint region of $Fe(acac)_3$ and $La(tmhd)_3$ for precursor powder from different stages of the flash-evaporation process. The pristine sample represents the initial powder bed before the synthesis, while the irradiated precursor consists of the residual material which is found inside the evaporation boat after 10 cycles. For both precursors, the FTIR spectra of the pristine and irradiated precursor are identical. This corresponds to

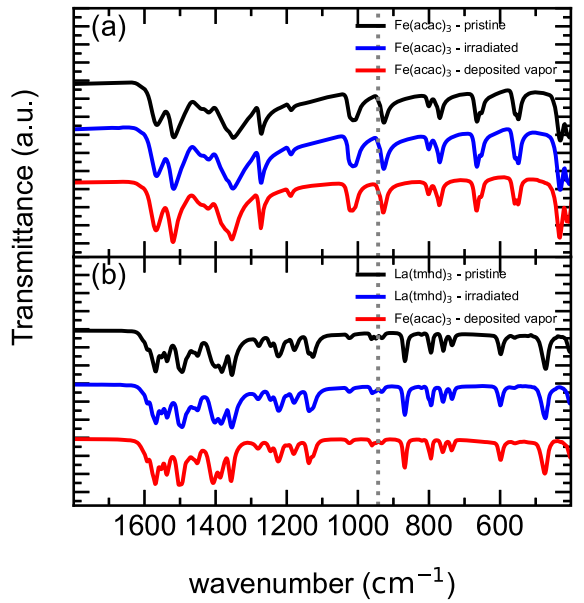

Fig. 3 FTIR spectra of the fingerprint region of $Fe(acac)_3$ and $La(tmhd)_3$ precursor at different stages of the CVS process. Dotted line marks emission of IR laser

the visual observation of a molten precursor inside the evaporation boat without signs of decomposition. The deposited vapors represent the precursor that is delivered into the reactor. Here, the $Fe(acac)_3$ spectra from the deposited and pristine vapor exhibit corresponding absorption bands. Hence, the spectra show no indication of a decomposition of $Fe(acac)_3$ molecules by flash-evaporation with a focused beam. The $La(tmhd)_3$ before and after flash-evaporation exhibit corresponding absorption bands. However, subtle changes in intensity are visible at 1460, 1130, and 950 cm^{-1}. The absorption band at 1460 cm^{-1} is assigned to the asymmetric in-plane bending of CH_3, while 1130 and 950 cm^{-1} corresponds to in-plane rocking vibrations of CH_3 [22]. Overall, the comparison of the FTIR data shows that both precursors are flash-evaporated by a focused laser beam without significant decomposition. Besides precursor stability, a key metric of a precursors system is the precise control of delivery rates. The measured evaporation rates of a stoichiometric $Fe(acac)_3$ and $La(tmhd)_3$ mixture as a function of the average laser power input are shown in Fig. 2b. The average power input is lowered by the time which the laser spends in an idle state during the repositioning at the end of a scanned line. As the power input increases and a threshold is passed, the evaporation rate rises proportionally. Furthermore, the deviation of individual runs is small resulting as indicated by the small margin of error. In summary, the focused beam of the marking head allows a decomposition-free evaporation, where the evaporation rate is precisely controlled by the power input.

$LaFeO_3$ nanoparticles

The CVS generation of $LaFeO_3$ is a suitable benchmark to examine the performance of the flash-evaporator. This synthesis requires high evaporation rates and the resulting particle characteristics are sensitive towards subtle changes in process parameters. Furthermore, both precursors exhibit different thermal behavior and the pure perovskite phase is only formed for a stoichiometric composition in the phase diagram [23]. Hence, a failure of the flash evaporator to deliver a steady stream of stoichiometric precursor vapors will result in a varying phase composition of the nanoparticles. Therefore, the structure of the synthesized nanoparticles is examined in detail to verify constant structural characteristics across the ensemble of particles.

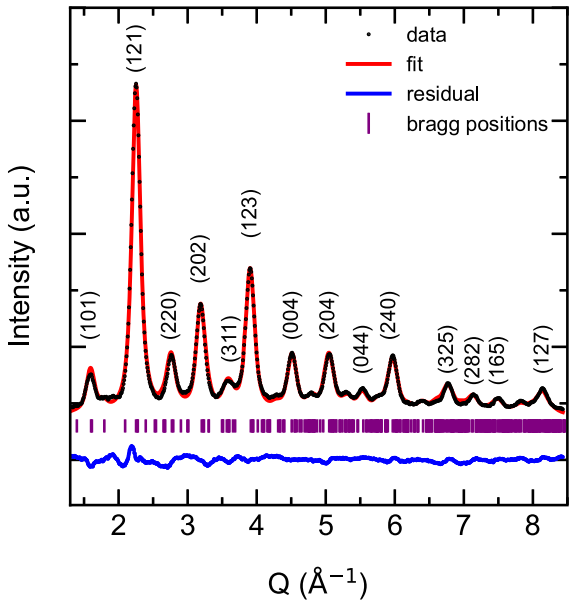

Fig. 4 X-ray diffractogram of nanocrystalline $LaFeO_3$ (λ = 0.02073 Å) including Rietveld refinement with corresponding Bragg positions

The X-ray diffractogram and corresponding Rietveld refinement of the $LaFeO_3$ nanoparticles are shown in Fig. 4. Overall, the prominent reflections correspond to the orthorhombic phase of $LaFeO_3$ [24] with space group Pnma (62) and exhibit a significantly broadened profile. Within the limits of Rietveld refinement, the fitted model matches the dataset and indicates the synthesis of phase-pure and stoichiometric $LaFeO_3$. The refined parameters from Rietveld analysis are listed in Table 1. Compared to the published phase, the unit cell is expanded to a volume of 245.18 $Å^3$ from the bulk value of 243.02 $Å^3$ which is typical for nanoscaled oxides [25]. Furthermore, the average crystallite size is refined to 5.25 nm with a microstrain of 0.65% which shows the nanocrystalline microstructure of the powder.

The HRTEM image of the $LaFeO_3$ nanoparticles in Fig. 5a and b shows highly crystalline and uniform nanoparticles with sizes in a narrow 5-nm size range. The SAED pattern of the nanoparticles

Table 1 Results of Rietveld refinements of XRD data of $LaFeO_3$ nanoparticles

Space group	*Pnma* (62)				
λ (Å)	0.2073				
a (Å)	5.620(2)				
b (Å)	7.849(6)				
c (Å)	5.559(4)				
	Symbol	x	y	z	B (Å^2)
La^{3+}	4c	0.4709	0.2500	0.0061	0.68
Fe^{3+}	4a	0.0000	0.0000	0.0000	0.45
O^{2-}	4c	0.5110	0.2500	0.5690	0.64
O^{2-}	8d	0.2190	0.0390	0.2800	2.24
d_{XRD} (nm)	5.25(6)				
ϵ (%)	0.64(20)				
R_{wp} (%)	2.02				
R_{exp} (%)	1.34				

The standard deviations in parentheses indicate refined parameters (a, b, c, lattice parameters; x, y, z, fractional coordinates; B, atomic temperature factor; d_{XRD}, coherent scattering column length (crystallite size); ϵ, microstrain; R, Rietveld fit indices)

is depicted in Fig. 5d and shows a ring diffraction pattern that originates from the superposition of the differently orientated crystallites. The integrated and background-subtracted electron diffractogram is plotted in Fig. 5c with the corresponding Bragg positions of the Rietveld refined unit cell of the $LaFeO_3$ phase using the X-ray diffractogram. The positions in Q-space of the reflections of the electron diffraction pattern are identical to the Bragg positions of the refined unit cell. Although consistent with XRD, the electron diffraction pattern exhibits significant differences in the intensity of reflections since electrons have different atomic form factors than X-rays. Furthermore, the more intense instrumental broadening of the TEM leads to broadened and overlapping reflections. Therefore, quantitative data analysis is performed only on X-ray diffraction data. Additionally, an elemental map from energy-dispersive X-ray spectroscopy (EDX) is provided in Fig. 8 in the Appendix. The HRTEM dataset confirms qualitatively the earlier findings of the XRD refinement. The constant structural characteristics of the ensemble confirm that the flash evaporator delivers a steady stream of precursors vapor over the whole duration of the synthesis. Larger particles or other byproducts are absent indicating that the focused beam solely sublimes the precursor without ablating solid chunks from the powder bed or preferential evaporation of one precursor.

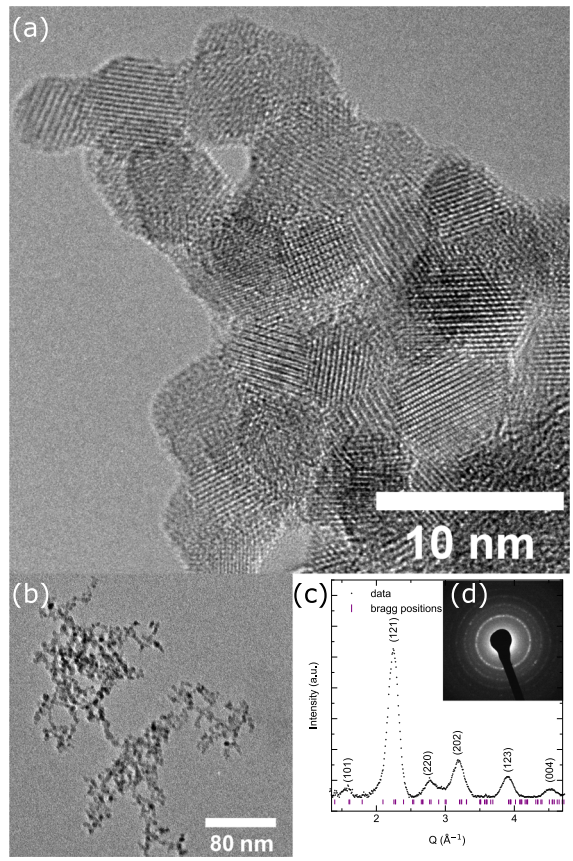

Fig. 5 TEM micrograph of $LaFeO_3$ (a) nanoparticles and (b) agglomerates. SAED pattern (d) with corresponding, integrated intensity (c)

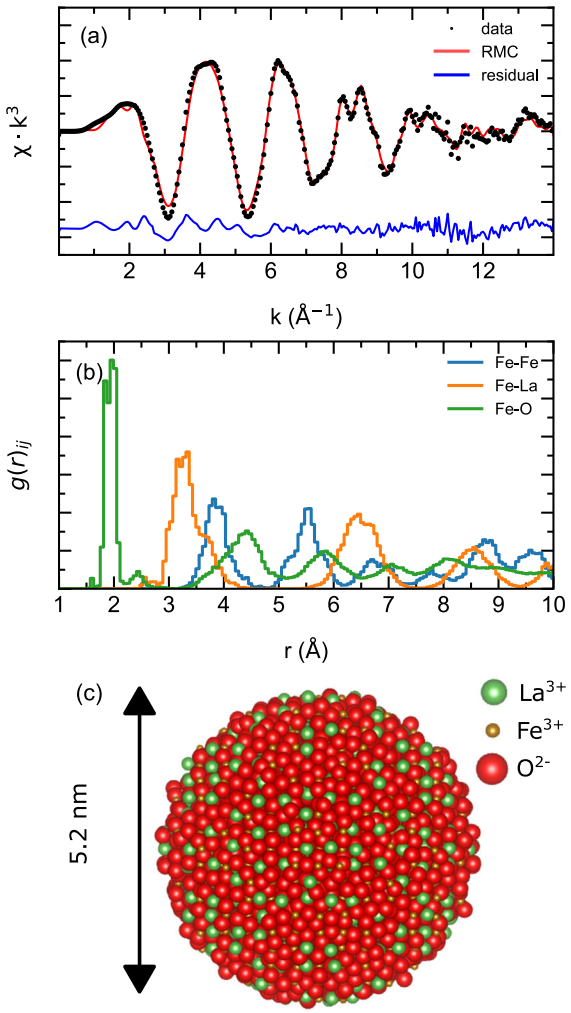

Fig. 6 RMC analysis consisting of (a) EXAFS Fe-K edge spectrum, (b) resulting pPDF, and (c) refined model of the $LaFeO_3$ nanoparticle

Figure 6a shows EXAFS at the Fe-K edge of the as synthesized nanoparticles and the simulated EXAFS spectrum of the refined RMC model. The corresponding spectra in *R*-space are provided in Fig. 9 in the Appendix. The spectrum of the refined model matches the measured data and only high frequency noise is left in the residual. The refined structural model of the nanoparticle itself is shown in Fig. 6c its partial pair distribution functions (pPDF) are shown in Fig. 6b. Besides thermal disorder which is represented by the broadened distribution of the pPDFs, the refined structure corresponds to the initial RMC model of the $LaFeO_3$ sphere which is provided in the supplementary Fig. 10 in the Appendix. For a quantitative comparison of the local structure, the parameters *N*, *R*, and σ^2 from the moment analysis are listed in Table 2. Here, the parameters from RMC are within the margin of error identical to the parameters from Rietveld refinement. In summary, RMC analysis confirms the constant structural characteristics of the nanoparticles synthesized by the flash evaporator setup.

Conclusion

In summary, the CVS process with the newly developed precursor delivery system which is based on a laser marking head produces highly crystalline and phase-pure nanoparticles of complex oxides with constant structural characteristics of the ensemble of particles. The energy density of the focused laser beam enables the stoichiometric sublimation of $Fe(acac)_3$ and $La(tmhd)_3$. Although the power density of the focused laser beam is an order of magnitude higher than in previously existing setups, the precursor sublimes without decomposition while the average power input is significantly reduced, compared to previously existing setups.

Table 2 Resulting parameters from pPDF moment analysis of refined RMC model and comparison to bulk reference

		RMC results			Reference		
Pair	Range (Å)	*N*	*R* (Å)	σ^2 (10^{-3}Å^2)	*N*	*r* (Å)	σ^2 (10^{-3}Å^2)
Fe-O	1.7–2.3	5.6(9)	2.009(1)	8(2)	6	2.009	24
Fe-La	3.1–3.7	7.1(18)	3.423(1)	27(9)	8	3.28–3.54	26
Fe-Fe	3.6–4.2	5.3(12)	3.949(1)	22(7)	6	3.93	17

Appendix

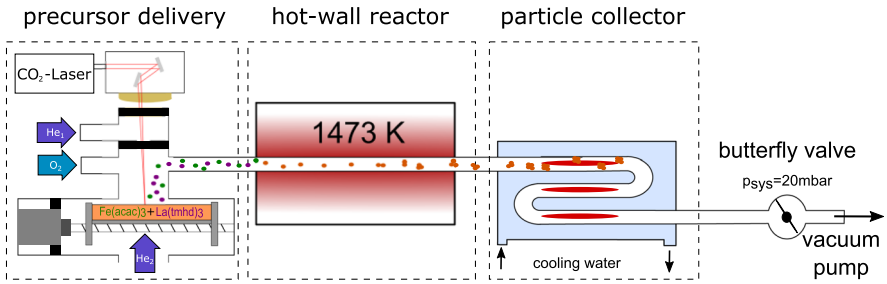

Fig. 7 Scheme of a CVS setup using a flash-evaporator with a scanning head laser to synthesize $LaFeO_3$. The dotted frames mark the sequential stages of the gas-phase process

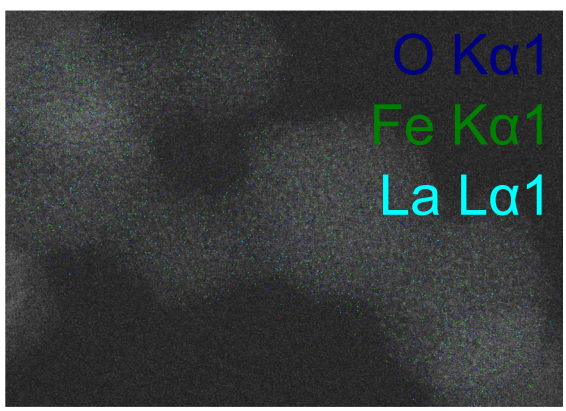

Fig. 8 Elemental map of $LaFeO_3$ nanoparticles from EDX. Elements are evenly distributed across the ensemble of nanoparticles

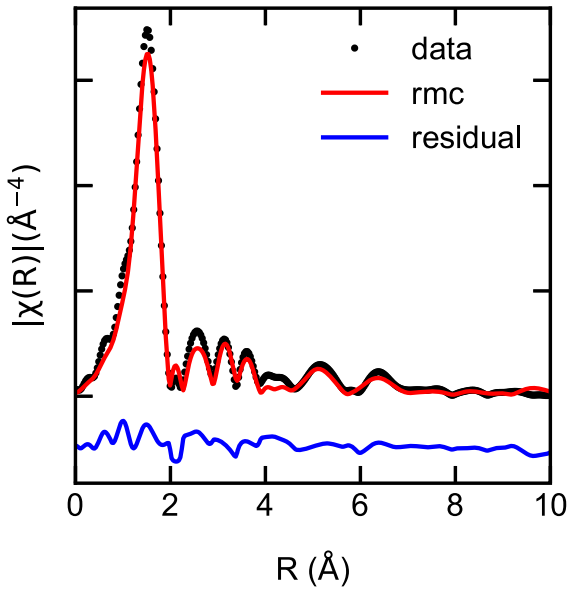

Fig. 9 Fourier transformed Fe-K(left) EXAFS spectrum (black), simulated EXAFS spectra of the refined model (red) and corresponding residual (blue)

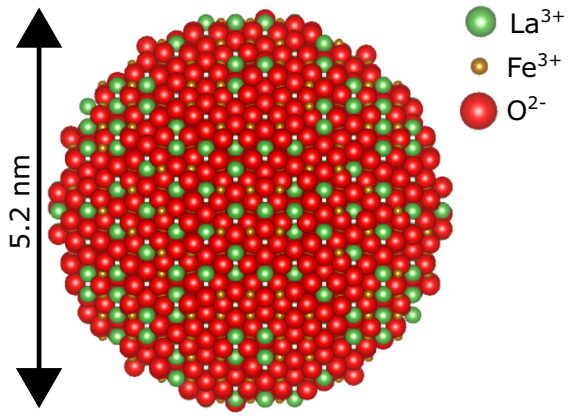

Fig. 10 Initial particle model for RMC analysis, based on Rietveld refinement of the $LaFeO_3$ nanoparticles

Acknowledgements This research used resources of the Advanced Photon Source, a US Department of Energy (DOE) Office of Science User Facility, operated for the DOE Office of Science by Argonne National Laboratory under Contract No. DE-AC02-06CH11357. We are very thankful for provision of XAS beamtime at beamline 20-BM-B through APS Staff-76323 and for the generous help by Chengjun Sun and Inhui Hwang. We acknowledge DESY (Hamburg, Germany), a member of the Helmholtz Association HGF, for the provision of experimental facilities. Parts of this research were carried out at PETRA III and we would like to thank Martin Etter for assistance in using P02.1. Beamtime was allocated for proposal RAt-20010294. Support by the Interdisciplinary Center for Analytics on the Nanoscale (ICAN) of the University of Duisburg-Essen (DFG RIsources reference: RI_00313), a DFG-funded core facility (Project Nos. 233512597 and 324659309), is gratefully acknowledged. We are thankful to Markus Heidelmann from the ICAN for help with the HRTEM measurements.

Author contribution Jeremias Geiss: conceptualization, methodology, investigation, data analysis, software, writing—original draft. Jeldrik Schulte: investigation, data analysis, manuscript formatting. Markus Winterer: supervision, reviewing and editing, resources.

Funding Open Access funding enabled and organized by Projekt DEAL. This research is funded by the Deutsche Forschungsgemeinschaft (DFG, German Research Foundation) – 388390466 – TRR 247 Project B1 and Project S.

Data availability The data that support the findings of this study are available from the corresponding author upon reasonable request.

Compliance with ethical standards

Ethics approval This article does not contain any studies with human participants or animals performed by any of the authors.

Consent for publication The authors have given consent for publication.

Conflict of interest The authors declare no competing interests.

References

1. Ismael M, Wark M (2019) Perovskite-type $LaFeO_3$: Photoelectrochemical properties and photocatalytic degradation of organic pollutants under visible light irradiation. Catalysts 9(4):342. https://doi.org/10.3390/catal9040342
2. Giannakas A, Ladavos A, Pomonis P (2004) Preparation, characterization and investigation of catalytic activity for NO+CO reaction of $LaMnO_3$ and $LaFeO_3$ perovskites prepared via microemulsion method. Appl Catal B 49(3):147–158. https://doi.org/10.1016/j.apcatb.2003.12.002
3. Kruis F, Fissan H, Peled A (1998) Synthesis of nanoparticles in the gas phase for electronic, optical and magnetic applications-a review. J Aerosol Sci 29(5-6):511–535. https://doi.org/10.1016/s0021-8502(97)10032-5
4. Malekzadeh M, Swihart MT (2021) Vapor-phase production of nanomaterials. Chem Soc Rev 50(12):7132–7249. https://doi.org/10.1039/d0cs01212b
5. Winterer M (2002) Nanocrystalline ceramics. Springer, Berlin.
6. O'Brien P, Pickett N, Otway D (2002) Developments in CVD delivery systems: a chemist's perspective on the chemical and physical interactions between precursors. Chem Vapor Depos 8(6):237–249. https://doi.org/10.1002/1521-3862(20021203)8:6<237::aid-cvde237>3.0.co;2-o
7. Winterer M, Srdic VV, Djenadic R et al (2007) Chemical vapor synthesis of nanocrystalline perovskites using laser flash evaporation of low volatility solid precursors. Rev Sci Instrum 78(12):123,903. https://doi.org/10.1063/1.2821234
8. Djenadic R, Akgül G, Attenkofer K et al (2010) Chemical vapor synthesis and structural characterization of nanocrystalline $Zn_{1-x}Co_xO$ (x = 0-0.50) particles by x-ray diffraction and x-ray absorption spectroscopy. J Phys Chem C 114(20):9207–9215. https://doi.org/10.1021/jp908148y
9. Djenadic R, Winterer M (2012) Chemical vapor synthesis of nanocrystalline oxides. In: Nanoparticles from the Gas-

phase. Springer, Berlin, pp 49–76. https://doi.org/10.1007/978-3-642-28546-2_2
10. Stijepovic I, Djenadic R, Srdic VV et al (2015) Chemical vapour synthesis of lanthanum gallium oxide nanoparticles. J Eur Ceram Soc 35(13):3545–3552. https://doi.org/10.1016/j.jeurceramsoc.2015.05.020
11. Loho C, Darbandi AJ, Djenadic R et al (2014) CO2-Laser flash evaporation as novel CVD precursor delivery system for functional thin film growth. Chem Vapor Depos 20(4-5-6):152–160. https://doi.org/10.1002/cvde.201307089
12. Fahlman BD, Barron AR (2000) Substituent effects on the volatility of metal β-diketonates. Adv Mater Opt Electr 10(3-5):223–232. https://doi.org/10.1002/1099-0712(200005/10)10:3/5<223::aid-amo411>3.0.co;2-m
13. Bedoya C, Condorelli G, Finocchiaro S et al (2006) MOCVD of lanthanum oxides from La(tmhd)$_3$ and La(tmod)$_3$ precursors: a thermal and kinetic investigation. Chem Vapor Depos 12(1):46–53. https://doi.org/10.1002/cvde.200506391
14. Siddiqi MA, Siddiqui RA, Atakan B (2007) Thermal stability, sublimation pressures and diffusion coefficients of some metal acetylacetonates. Surf Coat Technol 201(22-23):9055–9059. https://doi.org/10.1016/j.surfcoat.2007.04.036
15. Dippel AC, Liermann HP, Delitz JT et al (2015) Beamline p02.1 at PETRA III for high-resolution and high-energy powder diffraction. J Synchrotron Radiat 22(3):675–687. https://doi.org/10.1107/s1600577515002222
16. Prescher C, Prakapenka VB (2015) DIOPTAS: A program for reduction of two-dimensional x-ray diffraction data and data exploration. High Pressure Res 35(3):223–230. https://doi.org/10.1080/08957959.2015.1059835
17. Doebelin N, Kleeberg R (2015) Profex: a graphical user interface for the rietveld refinement program bgmn. J Appl Crystallogr 48(5):1573–1580. https://doi.org/10.1107/s1600576715014685
18. Heald SM, Brewe DL, Stern EA et al (1999) XAFS and micro-XAFS at the PNC-CAT beamlines. J Synchrotron Radiat 6(3):347–349. https://doi.org/10.1107/s090904959801677x
19. Winterer M (2020) Xafsx: a program to process, analyse and reduce x-ray absorption fine structure spectra XAFS. In: International Tables for Crystallography. International Union of Crystallography. https://doi.org/10.1107/s1574870720003481
20. Winterer M (2000) Reverse monte carlo analysis of extended x-ray absorption fine structure spectra of monoclinic and amorphous zirconia. J Appl Phys 88(10):5635–5644. https://doi.org/10.1063/1.1319167
21. Ankudinov AL, Ravel B, Rehr JJ et al (1998) Real-space multiple-scattering calculation and interpretation of x-ray-absorption near-edge structure. Phys Rev B 58(12):7565–7576. https://doi.org/10.1103/physrevb.58.7565
22. Vakili M, Tayyari S, Afzali R (2015) Conformation, molecular structure, and vibrational assignment of bis(2,2,6,6-tetramethylheptane-3,5-dionato)copper(II). Spectrochim Acta Part A 136:1827–1833. https://doi.org/10.1016/j.saa.2014.10.092
23. Moruzzi VL, Shafer MW (1960) Phase equilibria in the system La_2O_3-iron oxide in air. J Am Ceram Soc 43(7):367–372. https://doi.org/10.1111/j.1151-2916.1960.tb13673.x
24. Falcón H, Goeta A, Punte G et al (1997) Crystal structure refinement and stability of $LaFe_xNi_{1-x}O_3$ solid solutions. J Solid State Chem 133(2):379–385. https://doi.org/10.1006/jssc.1997.7477
25. Diehm PM, Ágoston P, Albe K (2012) Size-dependent lattice expansion in nanoparticles: reality or anomaly? ChemPhysChem 13(10):2443–2454. https://doi.org/10.1002/cphc.201200257